

Strain-Path Controlled Microstructure, Texture and Hardness Evolution in Cryo-Deformed AlCoCrFeNi_{2.1} Eutectic High Entropy Alloy

A. Patel¹, I. Wani¹, S.R. Reddy¹, S. Narayanswamy¹, A. Lozinko³, R. Saha², S. Guo³, P.P. Bhattacharjee^{1,*}

¹Department of Materials Science and Metallurgical Engineering
Indian Institute of Technology Hyderabad, Kandi, Sangareddy, 502285, Telangana, India.

²R&D Division, TATA Steel, Jamshedpur

³Chalmers University of Science and Technology

Abstract

The effect of strain path on microstructure, texture and hardness properties of AlCoCrFeNi_{2.1} eutectic high entropy alloy containing ordered FCC (L₁₂) and ordered BCC (B2) was investigated. The EHEA was cryo-rolled using UCR, MSCR (during which the samples were rotated by 90° around the ND between each pass) and TSCR(45°) (in which the samples were deformed by unidirectional rolling to half of the total strain and then diagonally rolled for rest half of the strain). The UCR processed material showed a rather heterogeneous microstructure. The textures of the L₁₂/FCC and B2 phases in the MSCR processed material agreed with the cross-rolling texture of the corresponding single phase materials, while the texture of the two phases in the TSCR(45°) processed materials appeared rather weak. Upon annealing at 800°C, the UCR processed materials showed a novel heterogeneous microstructure, while the MSCR and TSCR(45°) processed materials revealed microduplex structure. The heterogeneous microstructure was replaced by the usual microduplex structure at higher annealing temperatures. The annealing texture of the L₁₂/FCC phase showed the presence of α -fiber (ND//<011>) components while the B2 phase showed strong ND-fiber (ND//<111>) components. The UCR processed material with novel heterogeneous microstructure showed much greater hardness as compared to the MSCR and TSCR(45°) processed materials. The present results indicate that strain path exerted significant influence in controlling microstructure, texture and hardness properties of EHEA.

Keywords: High entropy alloys; strain path; cryo-rolling; microstructure; texture; hardness

*Corresponding author, Tel: +91 40 2301 6069, Email: pinakib@iith.ac.in

1. Introduction

High entropy alloys (HEAs) are a class of novel multicomponent alloys developed using the alloy design concept of mixing a large number (usually greater than five) of elements having concentrations varying from 5 to 35 at.% [1]. Despite their complex concentrated alloy chemistry, the HEAs may show rather simple microstructures, such as FCC (e.g. equiatomic CoCrFeMnNi [2]), BCC (e.g. refractory high entropy alloys WNbMoTa [3], WNbMoTaV [3] , FCC+BCC (e.g. Al_{0.5}CoCrFeMnNi [4]), or even HCP (e.g. GdHoLaTbY[5], YGdTbDyLu [6] and GdTbDyTmLu [6]). This is considered to be an effect of high configurational entropy of mixing of a large number of elements, which diminishes the free energy sufficiently to stabilize phases with simple crystal structures [1]. The emergence of HEAs has opened up the massive composition space of hyper-dimensional phase diagrams with the possibility of finding alloys with novel composition and unprecedented properties [7-15].

For a vast majority of engineering materials, development of appropriate thermo-mechanical processing (TMP) strategies are warranted [16-22] to enhance their properties in comparison to the as-cast materials [23, 24] [25-41]. The usual TMP treatments often involve heavy plastic straining and thermal annealing treatments, which influence microstructure and texture of the processed materials. Consequently, appropriate understanding of microstructure and texture development during TMP remains critical [42, 43] [44-48]. As a result, the effects of usual TMP parameters including plastic strain [16], grain size [49], cryo-rolling [21, 50] and heating rate [51] on microstructure and texture development in FCC equiatomic CoCrFeMnNi HEA have been clarified.

In addition to the usually investigated TMP parameters, strain-path remains an important aspect, which exerts considerable influence on microstructure, texture and properties. The effect of strain

path can be investigated by cross-rolling. Unlike unidirectional rolling, the rolling direction (RD) and transverse direction (TD) are mutually interchanged by the rotation of the sample around the normal direction (ND) [52]. The effect of different cross-rolling routes has been extensively investigated in conventional single phase [52-59], duplex [60, 61] and very recently in equiatomic CoCrFeMnNi HEA [62]. It has been reported that texture of cross-rolled FCC materials including aluminum and copper alloys [53-57], nickel [58, 63] and CoCrFeMnNi HEA [62] show significant differences with straight (or unidirectional) rolled materials featured by the gradual development of ND-rotated brass components. Development of unusual recrystallization texture components such as ND//<111> fiber texture in nickel [63], significant weakening or even complete randomization of texture [64] are observed upon annealing.

In the present research, we investigate for the first time the effect of strain-path on microstructure and texture in cryo-deformed AlCoCrFeNi_{2.1} eutectic high entropy alloy (EHEA). It is considered that deformation of multiphase alloys, particularly after cryo-rolling and annealing could lead to novel microstructure and properties. Further, the EHEA shows excellent workability, thus rendering them amply suitable for the present investigation. Further, the microstructure and texture due to cross-rolling has been studied to a very limited extent, notably in duplex brass [61] and duplex steel [60]. It is expected that the present research should be helpful in understanding the behavior of other multiphase materials including HEAs.

2. Experimental

2.1. Processing

The experimental AlCoCrFeNi_{2.1} EHEA was prepared by arc melting in a Ti-gettered high-purity argon atmosphere using high purity constituent metals ($\geq 99.9\%$). In order to achieve high quality melt with improved chemical homogeneity, the melting cycle was repeated no less than

five times. The molten alloy was suction-cast into a copper mold having inner dimensions of 15 mm (width) x 90 mm (length) x 3 mm (thickness). Specimens with dimensions 20 mm (long) x 15mm (width) x 3 mm (thickness)) were extracted from the as-cast EHEA and the surfaces are carefully prepared to remove any contamination.

The EHEA samples were deformed up to 90% reduction in thickness using different multistep cryo-rolling routes, schematically shown in Fig.1. During unidirectional cryo-rolling (UCR) (Fig.1(a)), the rolling direction (RD) was kept unchanged. During multistep cross-rolling (MSCR) (Fig.1(b)), the sheets were rotated by 90° about the normal direction (ND) after each pass. As a result, the RD and the transverse directions (TD) were interchanged in every pass. In the two-step cross-rolling (TSCR) route, the samples were first subjected to unidirectional deformation to half of the total equivalent strain ($\epsilon_{eq}/2 \sim 1.3$ corresponding to a thickness reduction of ~65%) along a fixed RD. Following this stage, further reduction in thickness to a total equivalent strain of ~2.65 (corresponding to 90% reduction in thickness) was carried out diagonally along 45° to the original RD. For this purpose, specimens were extracted by wire-cut electro discharge machining (EDM) along 45° to the RD of stage 1 (i.e. at $\epsilon_{eq}/2$). As a result, this route is designated as TSCR(45°) (Fig.1(c)). Evidently, the direction of rolling was changed only once (i.e. after stage 1 after a true equivalent strain of ~1.3) in the TSCR(45°) route. In all the different rolling routes, the samples were immersed in liquid N₂ for 30 minutes before and immediately after each rolling pass.

Small specimens obtained from the 90% cryo-rolled sheets prepared using the different rolling routes were annealed for 1 h at temperature ranging from 800°C to 1200°C. The annealed samples were immediately quenched in cold water following the heat treatments.

2.2 Characterization

The microstructure and texture of the cross-rolled material were investigated using electron backscatter diffraction (EBSD) system (Oxford Instruments, UK) attached to a FEG-SEM (Maker: Carl-Zeiss, Germany; Model: Supra 40). Since the deformed materials contained unindexed regions, the phase fractions in the deformed EHEA processed by the different rolling routes were determined from the SEM micrographs using the ImageJ open source image processing software [65]. The acquired EBSD dataset were analyzed by TSL-OIM™ (EDAX, USA) commercial software package. The samples for EBSD measurements were prepared by careful mechanical polishing using colloidal silica followed by electro-polishing at room temperature using a mixture of perchloric acid and methanol in a ratio of 1:9 (by volume). Several EBSD scans were obtained from different regions of each deformed and annealed specimens. These scans were merged for calculating the orientation distribution functions (ODFs). The ODFs were calculated using the series expansion method with series rank 22.

3. Results

3.1 Evolution of microstructure and texture during deformation

The microstructure of the EHEA shows lamellar arrangement of FCC and BCC phases [40, 41]. The volume fractions of the FCC and BCC phases (determined using EBSD) are ~ 65% and 35%, respectively, while the average thickness values are ~0.56 μm and 0.20 μm , respectively. TEM diffraction analysis has revealed that both these constituent phases have ordered structures [40, 41]. Fig.2 shows the SEM micrographs of the EHEA following 90% cryo-deformation by different rolling routes. The microstructure of the material processed by the UCR route (Fig.2(a)) shows lamellar regions (marked by yellow circles) elongated along the RD co-existing with fine fragmented regions (indicated by white circles). In stark contrast, the SEM micrographs of the

MSCR (Fig.2(b)) and TSCR(45°) (Fig.2(c)) processed materials clearly reveal remarkably fragmented B2 phase. The fragmented B2 phase show two kind of distinct morphologies, namely elongated and spherical. The maximum length of the elongated B2 phase may be several microns, while the fragmented spherical B2 phase appear to have a wide size range.

The remarkable differences in the microstructures of the three processed materials are amply corroborated by the EBSD image quality maps (IQ) (Fig.3). The IQ map of the UCR processed material (Fig.3(a)) depicts a narrow lamellar region (enclosed by circle) along with fine fragmented regions. The IQ maps of the MSCR (Fig.3(b)) and TSCR(45°) (Fig.3(c)) processed materials reveal the elongated morphology, however, unlike the UCR processed material, the microstructure is severely fragmented so that the lamellar eutectic regions could not be observed. During heavy deformation by cold [40, 41] and cryo-rolling [66], the L_{12} phase undergoes deformation induced disordering while the B2 phase retains the ordered structure. Therefore, the two phases are referred to as L_{12}/FCC and B2 phases in this work.

The phase fractions of the constituent L_{12}/FCC and BCC phases after 90% cryo-rolling by three different routes are compared in Fig.4. The phase fractions (determined using the ImageJ software) in the three processed materials are rather similar and do not show any significant differences with those in the as-cast EHEA.

The development of texture in the L_{12}/FCC phase of the 90% cryo-rolled materials processed by the three different routes are shown by the relevant ODF sections in Fig.5. The important deformation and recrystallization texture components in the L_{12}/FCC phase of the HEAs are summarized in Table 1. The $\varphi_2=0^\circ$ section of the ODF of the L_{12}/FCC phase in the UCR processed material (Fig.5(a)) shows strong intensities at $\varphi_1, \Phi, \varphi_2 = (25^\circ, 45^\circ, 0^\circ)$ in between the G and B_S locations, but somewhat shifted from the ideal B_S location. Presence of the Cu component is

evidenced in the $\varphi_2=45^\circ$ section of the ODF, while the S component is rather weak as may be observed from the $\varphi_2=65^\circ$ section. In contrast, the $\varphi_2=0^\circ$ section of the ODF of the $L1_2/FCC$ phase in the MSCR processed material (Fig.5(b)) shows the development of an α -fiber ($ND//\langle 110 \rangle$) with discrete intensity peaks at the G and exactly at the $\varphi_1, \Phi, \varphi_2 = (45^\circ, 45^\circ, 0^\circ)$ location corresponding to the B_S/BS^{ND} component $\{011\}\langle 755 \rangle$. The $\varphi_2=45^\circ$ section shows near complete absence of the Cu-component. The $\varphi_2=0^\circ$ section of the TSCR(45°) processed material (Fig.5(c)) only shows intensities at the vicinity of the G orientation but does not show the presence of the $\{011\}\langle 755 \rangle$ orientation unlike the MSCR processed material. Presence of an $(011)[\bar{1}\bar{2}2]$ orientation corresponding to $\varphi_1, \Phi, \varphi_2 = (66^\circ, 45^\circ, 0^\circ)$ along the α -fiber is also noticed. The $\varphi_2=45^\circ$ section confirms the absence of the Cu component in this case as well.

The texture of the B2 phase in the 90% cryo-rolled materials processed by the three different routes are shown by the $\varphi_2=45^\circ$ section of the ODFs in Fig.6. The $\varphi_2=45^\circ$ section of the ODF of the B2 phase in the UCR processed material (Fig.6(a)) shows slightly shifted $\{111\}\langle 011 \rangle$ component which lies at the intersection of the ND- and RD- fibers. In contrast, the $\varphi_2=45^\circ$ section of the ODF of the B2 phase in the 90% MSCR processed material (Fig.6(b)) shows a distinct $\{001\}\langle 110 \rangle$ component belonging to the RD-fiber. The intensities of the contour lines show that the texture is weakened after MSCR processing. The $\varphi_2=45^\circ$ section of the ODF of the B2 phase in the 90% TSCR(45°) processed material (Fig.6(c)) shows the absence of any predominant RD or ND-fiber components. The texture appears to be significantly weakened in this case. In essence, the texture is weakened in MSCR and TSCR(45°) processed materials.

3.2 Evolution of microstructure, texture and hardness during annealing

The development of microstructure in the 90% cryo-deformed materials after annealing is shown in Fig.7. The phase map of the UCR processed material after annealing at 800°C (Fig.7(a))

shows a remarkably heterogeneous microstructure featured by lamellar regions and non-lamellar regions containing of coarse B2 phase and ultrafine L1₂/FCC grains. The coarse B2 phase shows extensive LAGB network (highlighted by white lines) indicating that the B2 phase is not yet recrystallized. This heterogeneous microstructure is replaced by rather homogenous fine micro-duplex structures after annealing at 1000°C (Fig.7(b)) and 1200°C (Fig.7(c)). In stark contrast to the UCR processed material, the MSCR (Fig.7(d)) and TSCR(45°) (Fig.7(g)) processed materials show the development of ultrafine micro-duplex structure after annealing at 800°C. The micro-duplex structures are rather stable even after annealing at 1000°C and 1200°C.

The change in FCC phase fraction with annealing temperatures in the EHEA processed by the three different routes are shown in Fig.8(a). As already highlighted, the 90% cryo-deformed materials processed by the three different routes show very similar phase fractions. The L1₂/FCC phase fraction decreases in all the three processed materials after annealing at 800°C. However, the decrease in the L1₂/FCC phase fraction is significantly lower in the UCR processed material as compared to the EHEA processed by the other two routes. The L1₂/FCC phase fraction tends to increase with increasing annealing temperature in all the three processed materials. However, the UCR processed materials shows higher L1₂/FCC fraction after annealing at 1200°C, as compared to the MSCR and TSCR(45°) processed materials.

The evolution of hardness in the three processed materials also reveals remarkably different behavior (Fig.8(b)). The hardness of the EHEA is significantly increased as compared to the as-cast material after cryo-rolling by the three different routes. However, the hardness values in three processed material appears rather similar after 90% cryo-deformation. Remarkably, the hardness of the UCR processed material is much greater than those of the MSCR and TSCR(45°) processed

materials after annealing at 800°C. Following annealing at 1000°C and 1200°C, the EHEA processed by the three different routes again shows very similar hardness values.

The evolution of texture in the $L1_2$ /FCC phase is summarized in Fig.9. The $\varphi_2=0^\circ$ sections are shown to highlight the major changes in texture. The $\varphi_2=0^\circ$ section of the ODF of the UCR processed material annealed at 800°C (Fig.9(a)) shows intensity at the vicinity of the G component. The G component is strengthened with increasing annealing temperature (Fig.9(b)), however, upon further annealing at 1200°C, the G/B component emerge as the strongest recrystallization texture component (Fig.9(c)). In contrast, the MSCR processed sample annealed at 800°C (Fig.9(d)) appears to develop an α -fiber containing $\{011\} \langle 755 \rangle$ component. The $\{011\} \langle 755 \rangle$ component is strengthened with increasing annealing temperature (Fig.9(e) and Fig.9(f)). The TSCR(45°) processed sample also shows the development of a weak α -fiber after annealing at 800°C (Fig.9(g)). With increasing annealing temperature, the intensity spreading between B_s and BS^{ND} is particularly high ((Fig.9(h) and Fig.9(i)). The material annealed at 1200°C shows a strong peak midway at the $\{011\} \langle 755 \rangle$ location (Fig.9(i)).

The evolution of texture in the B2 phase is summarized in Fig.10. The $\varphi_2=0^\circ$ section of the ODF of the B2 phase in the UCR processed material annealed at 800°C (Fig.10(a)) shows presence of rotated cube components. However, the ODF of the B2 phase annealed at 1000°C (Fig.10(b)) shows the presence of usual RD and ND-fiber components. The ODF section in the 1200°C (Fig.10(c)) annealed material appears very similar to that of the 1000°C material, signifying no significant changes in texture. In case of MSCR processed material, the $\{001\} \langle 1\bar{1}0 \rangle$ component present in the deformed condition in the MSCR processed material persists after annealing 800°C (Fig.10(d)) along with a strong ND-fiber. The ND-fiber is strengthened with increasing annealing temperature (Fig.10(e) and Fig.10(f)). The texture of the B2 phase in the

TSCR(45°) material is rather weak in the 800°C annealed condition (Fig.10(g)), however, formation of a strong ND-fiber is observed in this case after annealing at 1000°C (Fig.10(h)) and 1200°C (Fig.10(i)).

4. Discussion

4.1 Evolution of deformation microstructure and texture

The analysis of phase fraction in 90% cryo-deformed EHEA processed by the different rolling routes show no significant differences. This clearly indicates that the evolution of microstructure and texture in the three processed materials is not affected by phase transformations. The SEM micrograph and EBSD IQ map of the UCR processed material show the retention of the lamellar regions inherited from the as cast microstructure of the EHEA along with the fragmented B2 phase. In contrast, MSCR and TSCR(45°) processing routes leads to severe fragmentation of the B2 phase. The observed differences in microstructures could be rationalized considering the behaviour of the two constituent phases. The careful nano-indentation mapping of the as-cast EHEA reveals that the B2 phase is much harder than the L1₂/FCC phase [67]. Consequently, during heavy cold-rolling, the L1₂/FCC phase is deformed to a much larger extent as compared to the harder B2 phase which is rather easily fragmented. Thus, the microstructure of the EHEA heavily cold-rolled by the UCR route at room temperature shows the formation of deformation induced ultrafine to nanocrystalline grains FCC phase but presence of the mechanically fragmented B2 phase. At the cryo-rolling temperature, the B2 phase is expected to be even harder than the L1₂/FCC phase, which should lead to more strain partitioning to the L1₂ phase. Thus, the fragmentation of the B2 phase is observed in the EHEA processed by all the three rolling routes. Since the rolling direction is maintained constant in the UCR processing route, the starting lamellar microstructure is not completely destroyed, so that the deformed microstructure shows the retention of the lamellar

regions inherited from the as cast microstructure of the EHEA. However, structural rotation due to change in strain path in the MSCR and TSCR(45°) processing routes results in a complete fragmentation of the microstructure.

The genesis of deformation texture is correlated with the relative stability of different orientations through the rotation field $\dot{R}(\dot{\varphi}_1, \dot{\varphi}, \dot{\varphi}_2)$ and the divergence of the rotation field $(div \dot{R} = \frac{\partial \dot{\varphi}_1}{\partial \varphi_1} + \frac{\partial \dot{\varphi}}{\partial \varphi} + \frac{\partial \dot{\varphi}_2}{\partial \varphi_2})$ [68, 69]. For a stable orientation: $\dot{R} = 0$ and $div(\dot{R}) = 0$. Hong et al [70] have shown that the orientation $\{011\} \langle 1\bar{1}1 \rangle$ (which is basically ND rotated B_S or B_S^{ND} orientation lying on the α -fiber corresponding to $\varphi_1, \Phi, \varphi_2 = (55^\circ, 45^\circ, 0^\circ)$) would be stable under cross-rolling due to its higher inverse rotation rate and large negative divergence. Thus, the α -fiber orientations will converge at the B_S orientation (stable orientation during unidirectional rolling) and then will further rotate away to the $\{011\} \langle 1\bar{1}1 \rangle$ orientation when the RD is rotated by 90°. Thus, the orientations will be oscillating between the B_S and B_S^{ND} ($\{011\} \langle 1\bar{1}1 \rangle$), converging at $\varphi_1, \Phi, \varphi_2 = (45^\circ, 45^\circ, 0^\circ)$ corresponding to the orientation $\{011\} \langle 755 \rangle$ (B_S/B_S^{ND}) lying at the middle of the two dynamically stable end orientations B_S and B_S^{ND} .

The deformation texture of the $L1_2/FCC$ phase in the UCR processed material shows clear presence of the B_S component. In contrast, the MSCR processed material shows the development of α -fiber with a strong intensity peak exactly at the B_S/B_S^{ND} or the $(011)[7\bar{5}5]$ location. Evidently, the deformation texture of the $L1_2/FCC$ phase agrees quite well with the theoretical calculations of Hong et al [70] and also with the cross-rolling texture of different FCC materials [56]. On the other hand, the $L1_2/FCC$ phase in the material processed by the TSCR(45°) route shows a G/B component and $(011)[1\bar{2}2]$ component lying on the α -fiber, which is different from the $\{011\} \langle 755 \rangle$ component predicted by Hong et al [70]. Applying the analogy of Hong et al [70] for predicting the origin of $\{011\} \langle 755 \rangle$ component in MSCR processed material, simple

rotation of the B_S component by 45° does not lead to the observed components in the TSCR(45°) material. A very similar behavior is observed for TSCR(45°) processed equiatomic CoCrFeMnNi HEA [62]. This argument has been further supported by the study on diagonally rolled Cu (45° rolling to the prior RD similar to the TSCCR(45°) route, but the strain in step 1 and step 2 are different than in the present study) which develops different texture than 90° cross-rolled materials [71].

The B2 phase in the UCR processed material shows a strong but slightly shifted $\{111\}\langle 011\rangle$ component which has been reported for some cold-rolled B2 phases. The MSCR processed material shows a distinct $\{001\}\langle 110\rangle$ component which is typically observed in cross-rolled BCC, such as ferrite in duplex steel [60] and can be followed from the stability analysis of deformation texture components in BCC materials. In contrast, the B2 phase in the TSCR(45°) shows rather weak texture. Thus, the textures of both $L_{1/2}$ /FCC and B2 phases are significantly different in the TSCR(45°) processed EHEA. It appears that a 45° rotation around the RD can affect the deformation and slip activities more fundamentally, leading to the observed differences in texture.

4.2 Evolution of annealed microstructure and texture

The EHEA processed by the UCR route shows remarkably heterogeneous microstructure comprising of fine lamellar and coarse non-lamellar regions after annealing at 800°C , while the MSCR and TSCR(45°) processed materials show rather homogenous microduplex structure. The fine lamellar regions observed in the annealed microstructure of the UCR processed material are already present in the deformed microstructure. Further, due to the deformation carried out at the cryo-rolling temperature, the strain is mostly partitioned to the softer $L_{1/2}$ /FCC phase as compared to the harder B2 phase. Consequently, the rather small accumulated strain in the B2 phase leads to insignificant driving force for recrystallization. Thus, the B2 phase undergoes recovery which is

evidenced by the presence of heavy LAGB network inside the grains, while the severely deformed $L1_2$ /FCC phase gives rise to ultrafine recrystallized grains. Upon annealing at higher temperatures, the lamellar regions in the UCR processed material are completely broken down to yield microduplex structure. In contrast, the strain-path change implemented in the MSCR and TSCR(45°) processing routes results in a severely fragmented microstructure. Upon recrystallization, the fragmented deformed microstructures lead to fine microduplex structure. Thus, the annealed microstructure in the three processed materials could be adequately explained on the basis of characteristics differences in the deformed microstructures.

In all the three processed materials, the $L1_2$ /FCC phase fraction decreases after annealing at 800°C but increases with increasing annealing temperature, indicating that the $L1_2$ /FCC phase becomes stable at higher annealing temperature. This trend is observed in cold-rolled EHEA [41] and also in dual phase HEAs, such as $\text{Al}_{0.5}\text{CoCrFeMnNi}$ [4], and could be understood from the fact that the phase fractions in duplex materials vary depending upon the annealing temperature. However, the materials processed by the three different routes show significantly different phase fractions upon annealing, although the phase fractions in the deformed conditions are rather similar. The phase fractions in the MSCR and TSCR(45°) materials are similar, while the UCR processed material shows significantly different fractions. This indicates that the equilibrium phase fractions are not attained for the combination of annealing temperature and time due to the differences in transformation kinetics, originating from the differences in the deformed microstructures.

The recrystallization texture in the $L1_2$ /FCC phase of the EHEA processed by the three different routes following annealing at 800°C is featured by the retention of the respective deformation texture components. Since the grain growth is rather limited at this temperature, the texture is

mainly influenced by the nucleation pattern in the three processed materials. The retention of deformation texture components after annealing has been interpreted in terms of more homogeneous nucleation or absence of preferential nucleation [16]. The apparent similarities in the formation of texture components indicate similar mechanism. The respective texture components are strengthened at higher annealing temperatures due to grain growth.

The annealing texture of the B2 phase in the UCR processed material shows the usual RD and ND-fiber components. The ND fiber is strengthened, particularly after annealing at higher temperatures, as expected for the recrystallization texture of BCC materials. Development of strong ND-fiber is observed even in MSCR and TSCR(45°) processed materials, particularly at higher annealing temperatures. Thus, formation of ND-fiber is preferred irrespective of the processing routes. The presence of strong ND-fiber in the recrystallization texture of BCC materials is usually attributed to greater stored energy of the former [24]. It appears that this mechanism is also responsible for very similar recrystallization texture in the B2 phase dominated by ND-fiber, even though the deformation texture may show characteristic differences already highlighted.

The UCR processed material shows much greater hardness as compared to the MSCR and TSCR(45°) processed material after annealing at 800°C, although the hardness values of the EHEA processed by the three different routes are rather similar in the deformed state. The remarkable difference in the hardness originates from the novel heterogeneous microstructure [72] [73] of the UCR processed and annealed material. As has been clarified recently, the heterogeneous microstructure of the UCR processed and annealed (800°C/1 h) material is composed of different hardness domains, which lead to significant back stress strengthening, resulting in simultaneous enhancement in strength and ductility [62]. At higher annealing temperatures, the heterogeneous

microstructure transforms into microduplex structure, quite similar to the EHEA processed by the two other processing routes. This leads to very similar hardness values in the EHEA processed by the three different routes at annealing temperature beyond 800°C.

5. Conclusions

The main conclusions that may be drawn are:

- (i) The UCR processed materials show retention of lamellar regions as opposed completely fragmented microstructure in the MSCR and TSCR(45°) processed material.
- (ii) The development of the B_S^{ND} component in the $L1_2/FCC$ phase of the MSCR processed material agrees quite well with the texture of cross-rolled single phase $L1_2/FCC$ derived. However, the texture of the $L1_2/FCC$ phase in the TSCR(45°) processed material shows significant differences, indicating fundamental differences in deformation pattern.
- (iii) The texture of the B2 phase in the MSCR processed material shows a distinct $\{001\}\langle 110 \rangle$ component, which is in good agreement with cross-rolled texture of single phase BCC materials. In the TSCR(45°) material, the texture of the B2 phase is much weaker.
- (iv) Annealing of the UCR processed material at 800°C results in a remarkably heterogeneous microstructure as opposed to rather homogenous microduplex structure of the MSCR and TSCR(45°) processed materials. However, following annealing at 1000°C and 1200°C, the EHEA processed by the three different routes show very similar duplex structure.

- (v) The heterogeneous microstructure of the UCR processed material results in much greater hardness as compared to the MSCR and TSCR(45°) processed materials annealed at the same temperature of 800°C for 1 h. The materials processed by the three different routes shows no significant difference in hardness after annealing at 1000°C and 1200°C, concomitant with the transformation of the heterogeneous structure of the UCR processed material into duplex structure.
- (vi) The annealing texture of the L1₂/FCC phase shows presence of α -fiber components and is featured by the retention of the respective deformation texture components. The B2 phase shows strong ND-fiber texture, which is the usual recrystallization texture of the BCC materials.

Acknowledgements

The financial support DST, India (EMR/2016/002215) and Junior Researcher Grant from the Swedish Research Council under grant 2015-04087 are sincerely acknowledged.

List of Tables

Table 1: Important deformation and recrystallization texture components in L1₂/FCC phases.

Table 2: Important deformation and recrystallization texture components in B2 phase.

List of Figures

Fig.1: Schematic showing (a) UCR, (b) MSCR and (c) TSCR(45°) processing routes.

Fig.2: SEM micrographs of 90% cryo-rolled EHEA processed by (a) UCR, (b) MSCR and (c) TSCR(45°) processing routes.

Fig.3: EBSD IQ maps of 90% cryo-rolled EHEA processed by (a) UCR, (b) MSCR and (c) TSCR(45°) processing routes.

Fig.4: Phase fractions in as-cast and 90% cryo-deformed EHEA processed by different rolling routes.

Fig.5: Relevant ODF sections of the L1₂/FCC phase in 90% cryo-rolled EHEA processed by (a) UCR, (b) MSCR and (c) TSCR(45°) processing routes (for legends, refer to Table 1).

Fig.6: $\varphi_2=45^\circ$ section ODFs of the B2 phase in 90% cryo-rolled EHEA processed by (a) UCR, (b) MSCR and (c) TSCR(45°) processing routes (for legends, refer to Table 2). The intensities of the contour lines are same as in Fig.5.

Fig.7: EBSD phase map of EHEA processed by ((a)-(c)) UCR, ((d)-(f)) MSCR and ((g)-(i)) TSCR(45°) following annealing at ((a), (d), (g)) 800°C, ((b), (e), (h)) 1000°C and ((c), (f), (i)) 1200°C.

Fig.8: (a) Change in phase fraction and (b) hardness with annealing temperature in the EHEA processed by the three different routes.

Fig.9: $\varphi_2=0^\circ$ ODF sections of the L1₂/FCC phase in annealed EHEA processed by different routes (for legends, refer to Table 1). The intensities of the contour lines are same as in Fig.5.

Fig.10: $\varphi_2=45^\circ$ section of the ODFs of the B2 phase in annealed EHEA processed by different routes (for legends, refer to Table 2).

References

- [1] J.W. Yeh, S.K. Chen, S.J. Lin, J.Y. Gan, T.S. Chin, T.T. Shun, C.H. Tsau, S.Y. Chang, Nanostructured high-entropy alloys with multiple principal elements: Novel alloy design concepts and outcomes, *Adv. Eng. Mater.* 6 (2004) 299-303.
- [2] B. Cantor, I.T.H. Chang, P. Knight, A.J.B. Vincent, Microstructural development in equiatomic multicomponent alloys, *Mater. Sci. Eng. A* 375-377 (2004) 213-218.
- [3] O.N. Senkov, G.B. Wilks, D.B. Miracle, C.P. Chuang, P.K. Liaw, Refractory high-entropy alloys, *Intermetallics* 18 (2010) 1758-1765.
- [4] I.S. Wani, G.D. Sathiaraj, M.Z. Ahmed, S.R. Reddy, P.P. Bhattacharjee, Evolution of microstructure and texture during thermo-mechanical processing of a two phase Al_{0.5}CoCrFeMnNi high entropy alloy, *Mater. Charact.* 118 (2016) 417-424.
- [5] Y.J. Zhao, J.W. Qiao, S.G. Ma, M.C. Gao, H.J. Yang, M.W. Chen, Y. Zhang, A hexagonal close-packed high-entropy alloy: The effect of entropy, *Mater. Des.* 96 (2016) 10-15.
- [6] A. Takeuchi, K. Amiya, T. Wada, K. Yubuta, W. Zhang, High-Entropy Alloys with a Hexagonal Close-Packed Structure Designed by Equi-Atomic Alloy Strategy and Binary Phase Diagrams, *JOM* 66 (2014) 1984-1992.

- [7] Y. Zhang, T.T. Zuo, Z. Tang, M.C. Gao, K.A. Dahmen, P.K. Liaw, Z.P. Lu, Microstructures and properties of high-entropy alloys, *Prog. Mater. Sci.* 61 (2014) 1-93.
- [8] J.W. Yeh, Alloy Design Strategies and Future Trends in High-Entropy Alloys, *JOM* 65 (2013) 1759-1771.
- [9] B. Gludovatz, A. Hohenwarter, D. Catoor, E.H. Chang, E.P. George, R.O. Ritchie, A fracture-resistant high-entropy alloy for cryogenic applications, *Science* 6201 (2014) 1153-1158.
- [10] Y. Zhang, T. Zuo, Y. Cheng, P.K. Liaw, High-entropy alloys with high saturation magnetization, electrical resistivity, and malleability, *Sci. Rep.* 3 (2013) 1455.
- [11] M.H. Tsai, J.W. Yeh, High-entropy alloys: a critical review, *Mater. Res. Lett.* 2 (2014) 107-123.
- [12] D.B. Miracle, J.D. Miller, O.N. Senkov, C. Woodward, M.D. Uchic, J. Tiley, Exploration and Development of High Entropy Alloys for Structural Applications, *Entropy* 16 (2014) 494-525.
- [13] Y. Lu, Y. Dong, S. Guo, L. Jiang, H. Kang, T. Wang, B. Wen, Z. Wang, J. Jie, Z. Cao, H. Ruan, T. Li, A Promising New Class of High-Temperature Alloys: Eutectic High-Entropy Alloys, *Sci. Rep.* 4 (2014) 6200.
- [14] S.R. Reddy, S. Bapari, P.P. Bhattacharjee, A.H. Chokshi, Superplastic-like flow in a fine-grained equiatomic CoCrFeMnNi high-entropy alloy, *Mater. Res. Lett.* 5 (2017) 408-414.
- [15] W. Liu, Z. Lu, J. He, J. Luan, Z. Wang, B. Liu, Y. Liu, M. Chen, C. Liu, Ductile CoCrFeNiMo_x high entropy alloys strengthened by hard intermetallic phases, *Acta Mater.* 116 (2016) 332-342.
- [16] P.P. Bhattacharjee, G.D. Sathiaraj, M. Zaid, J.R. Gatti, C. Lee, C.W. Tsai, J.W. Yeh, Microstructure and texture evolution during annealing of equiatomic CoCrFeMnNi high-entropy alloy, *J. Alloy. Compd.* 587 (2014) 544-552.
- [17] F. Otto, N.L. Hanold, E.P. George, Microstructural evolution after thermomechanical processing in an equiatomic, single-phase CoCrFeMnNi high-entropy alloy with special focus on twin boundaries, *Intermetallics* 54 (2014) 39-48.
- [18] D.G. Shaysultanov, N.D. Stepanov, A.V. Kuznetsov, G.A. Salishchev, O.N. Senkov, Phase Composition and Superplastic Behavior of a Wrought AlCoCrCuFeNi High-Entropy Alloy, *JOM* 65 (2013) 1815-1828.
- [19] A.V. Kuznetsov, D.G. Shaysultanov, N.D. Stepanov, G.A. Salishchev, O.N. Senkov, Tensile properties of an AlCrCuNiFeCo high-entropy alloy in as-cast and wrought conditions, *Mater. Sci. Eng. A* 533 (2012) 107-118.
- [20] C.W. Tsai, M.H. Tsai, J.W. Yeh, C.C. Yang, Effect of temperature on mechanical properties of Al_{0.5}CoCrCuFeNi wrought alloy, *J. Alloy. Compd.* 490 (2010) 160-165.
- [21] N. Stepanov, M. Tikhonovsky, N. Yurchenko, D. Zyabkin, M. Klimova, S. Zherebtsov, A. Efimov, G. Salishchev, Effect of cryo-deformation on structure and properties of CoCrFeNiMn high-entropy alloy, *Intermetallics* 59 (2015) 8-17.
- [22] N. Park, I. Watanabe, D. Terada, Y. Yokoyama, P.K. Liaw, N. Tsuji, Recrystallization Behavior of CoCrCuFeNi High-Entropy Alloy, *Metal. Mater. Trans. A* 46 (2015) 1481-1487.

- [23] B. Verlinden, J. Driver, I. Samajdar, R.D. Doherty, *Thermo-Mechanical Processing of Metallic Materials*, Elsevier Science, Oxford, 2007.
- [24] F.J. Humphreys, M. Hatherly, *Recrystallization and Related Annealing Phenomena (Second Edition)*, Elsevier, Oxford, 2004.
- [25] C. Zhu, Z.P. Lu, T.G. Nieh, Incipient plasticity and dislocation nucleation of FeCoCrNiMn high-entropy alloy, *Acta Mater.* 61 (2013) 2993-3001.
- [26] Z. Wu, H. Bei, G.M. Pharr, E.P. George, Temperature dependence of the mechanical properties of equiatomic solid solution alloys with face-centered cubic crystal structures, *Acta Mater.* 81 (2014) 428-441.
- [27] J.Y. He, C. Zhu, D.Q. Zhou, W.H. Liu, T.G. Nieh, Z.P. Lu, Steady state flow of the FeCoNiCrMn high entropy alloy at elevated temperatures, *Intermetallics* 55 (2014) 9-14.
- [28] F. Otto, A. Dlouhý, C. Somsen, H. Bei, G. Eggeler, E.P. George, The influences of temperature and microstructure on the tensile properties of a CoCrFeMnNi high-entropy alloy, *Acta Mater.* 61 (2013) 5743-5755.
- [29] Z. Wu, H. Bei, F. Otto, G.M. Pharr, E.P. George, Recovery, recrystallization, grain growth and phase stability of a family of FCC-structured multi-component equiatomic solid solution alloys, *Intermetallics* 46 (2014) 131-140.
- [30] J. Antonaglia, X. Xie, Z. Tang, C.W. Tsai, J.W. Qiao, Y. Zhang, M.O. Laktionova, E.D. Tabachnikova, J.W. Yeh, O.N. Senkov, M.C. Gao, J.T. Uhl, P.K. Liaw, K.A. Dahmen, Temperature Effects on Deformation and Serration Behavior of High-Entropy Alloys (HEAs), *JOM* 66 (2014) 2002-2008.
- [31] Y. Zou, S. Maiti, W. Steurer, R. Spolenak, Size-dependent plasticity in an Nb₂₅Mo₂₅Ta₂₅W₂₅ refractory high-entropy alloy, *Acta Mater.* 65 (2014) 85-97.
- [32] M.A. Hemphill, T. Yuan, G.Y. Wang, J.W. Yeh, C.W. Tsai, A. Chuang, P.K. Liaw, Fatigue behavior of Al_{0.5}CoCrCuFeNi high entropy alloys, *Acta Mater.* 60 (2012) 5723-5734.
- [33] W.H. Liu, Y. Wu, J.Y. He, T.G. Nieh, Z.P. Lu, Grain growth and the Hall-Petch relationship in a high-entropy FeCrNiCoMn alloy, *Scr. Mater.* 68 (2013) 526-529.
- [34] Y. Wu, W.H. Liu, X.L. Wang, D. Ma, A.D. Stoica, T.G. Nieh, Z.B. He, Z.P. Lu, In-situ neutron diffraction study of deformation behavior of a multi-component high-entropy alloy, *Appl. Phys. Lett.* 104 (2014) 051910.
- [35] C.C. Tasan, Y. Deng, K.G. Pradeep, M.J. Yao, H. Springer, D. Raabe, Composition Dependence of Phase Stability, Deformation Mechanisms, and Mechanical Properties of the CoCrFeMnNi High-Entropy Alloy System, *JOM* 66 (2014) 1993-2001.
- [36] M.J. Yao, K.G. Pradeep, C.C. Tasan, D. Raabe, A novel, single phase, non-equiatomic FeMnNiCoCr high-entropy alloy with exceptional phase stability and tensile ductility, *Scr. Mater.* 72-73 (2014) 5-8.
- [37] C.W. Tsai, Y.L. Chen, M.H. Tsai, J.W. Yeh, T.T. Shun, S.K. Chen, Deformation and annealing behaviors of high-entropy alloy Al_{0.5}CoCrCuFeNi, *J. Alloy. Compd.* 486 (2009) 427-435.

- [38] Y.F. Kao, T.J. Chen, S.K. Chen, J.W. Yeh, Microstructure and mechanical property of as-cast, -homogenized, and -deformed $\text{Al}_x\text{CoCrFeNi}$ ($0 \leq x \leq 2$) high-entropy alloys, *J. Alloy. Compd.* 488 (2009) 57-64.
- [39] N. Nayan, G. Singh, S.V.S.N. Murty, A.K. Jha, B. Pant, K.M. George, U. Ramamurty, Hot deformation behaviour and microstructure control in AlCrCuNiFeCo high entropy alloy, *Intermetallics* 55 (2014) 145-153.
- [40] I.S. Wani, T. Bhattacharjee, S. Sheikh, Y.P. Lu, S. Chatterjee, P.P. Bhattacharjee, S. Guo, N. Tsuji, Ultrafine-Grained $\text{AlCoCrFeNi}_{2.1}$ Eutectic High-Entropy Alloy, *Mater. Res. Lett.* 4 (2016) 174-179.
- [41] I.S. Wani, T. Bhattacharjee, S. Sheikh, P.P. Bhattacharjee, S. Guo, N. Tsuji, Tailoring nanostructures and mechanical properties of $\text{AlCoCrFeNi}_{2.1}$ eutectic high entropy alloy using thermo-mechanical processing, *Mater. Sci. Eng. A* 675 (2016) 99-109.
- [42] R.D. Doherty, D.A. Hughes, F.J. Humphreys, J.J. Jonas, D.J. Jensen, M.E. Kassner, W.E. King, T.R. McNelley, H.J. McQueen, A.D. Rollett, Current issues in recrystallization: a review, *Mater. Sci. Eng. A* 238 (1997) 219-274.
- [43] D. Roger D, Recrystallization and texture, *Prog. Mater. Sci.* 42 (1997) 39-58.
- [44] P.P. Bhattacharjee, R.K. Ray, A. Upadhyaya, Recrystallization textures of powder metallurgically prepared pure Ni, Ni-W and Ni-Mo alloy tapes for use as substrates for coated superconductors, *Phy. C* 449 (2006) 116-121.
- [45] P.P. Bhattacharjee, M. Zaid, G. Sathiaraj, B. Bhadak, Evolution of microstructure and texture during warm rolling of a duplex steel, *Metall. Mater. Trans. A* 45 (2014) 2180-2191.
- [46] J. Hou, M. Zhang, S. Ma, P.K. Liaw, Y. Zhang, J. Qiao, Strengthening in $\text{Al}_{0.25}\text{CoCrFeNi}$ high-entropy alloys by cold rolling, *Mater. Sci. Eng. A* 707 (2017) 593-601.
- [47] Z. Wang, M.C. Gao, S.G. Ma, H.J. Yang, Z.H. Wang, M. Ziomek-Moroz, J.W. Qiao, Effect of cold rolling on the microstructure and mechanical properties of $\text{Al}_{0.25}\text{CoCrFe}_{1.25}\text{Ni}_{1.25}$ high-entropy alloy, *Mater. Sci. Eng. A* 645 (2015) 163-169.
- [48] J. Hou, M. Zhang, H. Yang, J. Qiao, Deformation Behavior of $\text{Al}_{0.25}\text{CoCrFeNi}$ High-Entropy Alloy after Recrystallization, *Metals* 7 (2017) 111.
- [49] P.P. Bhattacharjee, N. Tsuji, R.K. Ray, Effect of Initial Grain Size on the Evolution of $\{001\}\langle 100 \rangle$ Texture in Severely Deformed and Annealed High-Purity Nickel, *Metall. Mater. Trans. A* 42A (2011) 2769-2780.
- [50] G.D. Sathiaraj, P.P. Bhattacharjee, C.W. Tsai, J.W. Yeh, Effect of heavy cryo-rolling on the evolution of microstructure and texture during annealing of equiatomic CoCrFeMnNi high entropy alloy, *Intermetallics* 69 (2016) 1-9.
- [51] G.D. Sathiaraj, C.W. Tsai, J.W. Yeh, M. Jahazi, P.P. Bhattacharjee, The effect of heating rate on microstructure and texture formation during annealing of heavily cold-rolled equiatomic CoCrFeMnNi high entropy alloy, *J. Alloy. Compd.* 688 (2016) 752-761.
- [52] S. Suwas, A.K. Singh, Role of strain path change in texture development, *Mater. Sci. Eng. A* 356 (2003) 368-371.

- [53] C.Y. Chung, Earring control by delayed cross rolling, Proceedings of the Eleventh International Conference on Textures of Materials (1996) 711-716.
- [54] S. Suwas, A.K. Singh, K.N. Rao, T. Singh, Effect of modes of rolling on evolution of texture in pure copper and some copper base alloys - Part III: Yield locus anisotropy, *Z Metallkd* 94 (2003) 1313-1319.
- [55] T. Öztürk, Deformation and recrystallization textures in cross-rolled sheets of copper and α -brass, *Scr. Metall.* 22 (1988) 1611-1616.
- [56] N.P. Gurao, S. Sethuraman, S. Suwas, Effect of strain path change on the evolution of texture and microstructure during rolling of copper and nickel, *Mater. Sci. Eng. A* 528 (2011) 7739-7750.
- [57] S. Suwas, A.K. Singh, K.N. Rao, T. Singh, Effect of modes of rolling on evolution of the texture in pure copper and some copper-base alloys, *Z Metallkd* 93 (2002) 918-927.
- [58] P.P. Bhattacharjee, M. Joshi, V.P. Chaudhary, M. Zaid, The effect of starting grain size on the evolution of microstructure and texture in nickel during processing by cross-rolling, *Mater. Charact.* 76 (2013) 21-27.
- [59] J. Gubicza, Q.H. Bui, F. Fellah, N. Szasz, G. Dirras, Bulk ultrafine-grained Nickel consolidated from nanopowders, *Mater. Sci. Forum* 589 (2008) 93-98.
- [60] M. Zaid, P.P. Bhattacharjee, Electron backscatter diffraction study of deformation and recrystallization textures of individual phases in a cross-rolled duplex steel, *Mater. Charact.* 96 (2014) 263-272.
- [61] R. Garg, N.P. Gurao, S. Ranganathan, S. Suwas, Evolution of texture and grain boundary microstructure in two-phase (α plus β) brass during recrystallization, *Philos. Mag.* 91 (2011) 4089-4108.
- [62] S.R. Reddy, M.Z. Ahmed, G.D. Sathiaraj, P.P. Bhattacharjee, Effect of strain path on microstructure and texture formation in cold-rolled and annealed FCC equiatomic CoCrFeMnNi high entropy alloy, *Intermetallics* 87 (2017) 94-103.
- [63] P.P. Bhattacharjee, M. Joshi, V.P. Chaudhary, J.R. Gatti, M. Zaid, Texture Evolution During Cross Rolling and Annealing of High-Purity Nickel, *Metall. Mater. Trans. A* 44A (2013) 2707-2716.
- [64] M.Y. Huh, S.Y. Cho, O. Engler, Randomization of the annealing texture in aluminum 5182 sheet by cross-rolling, *Mater. Sci. Eng. A* 315 (2001) 35-46.
- [65] C.A. Schneider, W.S. Rasband, K.W. Eliceiri, NIH Image to ImageJ: 25 years of image analysis, *Nature Methods* 9 (2012) 671.
- [66] D.L. Abernathy, M.B. Stone, M.J. Loguillo, M.S. Lucas, O. Delaire, X. Tang, J.Y.Y. Lin, B. Fultz, Design and operation of the wide angular-range chopper spectrometer ARCS at the Spallation Neutron Source, *Rev. Sci. Instrum.* 83 (2012) 015114.
- [67] I.S. Wani, T. Bhattacharjee, S. Sheikh, I. Clark, M. Park, T. Okawa, S. Guo, P.P. Bhattacharjee, N. Tsuji, Cold-rolling and recrystallization textures of a nano-lamellar AlCoCrFeNi_{2.1} eutectic high entropy alloy, *Intermetallics* 84 (2017) 42-51.

- [68] J. Savoie, J.J. Jonas, Simulation of the deformation textures induced by deep drawing in extra low carbon steel sheets, *Acta Metall.* 42 (1994) 4101-4116.
- [69] L.S. Toth, J.J. Jonas, D. Daniel, R.K. Ray, Development of Ferrite Rolling Textures in Low-Carbon and Extra Low-Carbon Steels, *Metall. Trans. A* 21 (1990) 2985-3000.
- [70] S.H. Hong, D.N. Lee, Deformation and recrystallization textures in cross-rolled copper sheet, *J. Eng. Mater. Technol.* 124 (2002) 13-22.
- [71] M. Ostafin, J. Pospiech, R.A. Schwarzer, Microstructure and texture in copper sheets after reverse and cross rolling, *Solid State Phenomena, Trans. Tech. Publ.* 105 (2005) 309-314.
- [72] X. Wu, Y. Zhu, Heterogeneous materials: a new class of materials with unprecedented mechanical properties, *Mater. Res. Lett.* 5 (2017) 527-532.
- [73] X. Wu, M. Yang, F. Yuan, G. Wu, Y. Wei, X. Huang, Y. Zhu, Heterogeneous lamella structure unites ultrafine-grain strength with coarse-grain ductility, *Proc. Natl. Acad. Sci.* 112 (2015) 14501-14505.

Table 1: Important deformation and recrystallization texture components in L1₂/FCC phase.







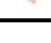











Texture component	Symbol	Euler angle (°)			Miller Indices
		Φ_1	Φ	Φ_2	
Cube (C)		0, 0, 0			{001} <100>
Copper (Cu)		90,35,45			{112} <111>
S		59,37,63			{123} <634>
Bs		35,45,0			{110} <112>
G		0,45,0			{110} <001>
Rt-G		90,45,0			{110} <110>
G/B		17,45,0			{110} <115>
B _s /B _s ND		45,45,0			{110} <755>
B _s ND		55,45,0			{110} <111>
BR		80,31,34			{236} <385>
D		90,25,45			{113} <332>
K		27,64,14			{142} <211>
M		80,30,65			{13 6 25} <20 15 14>

Table 2: Important deformation and recrystallization texture components in B2 phase.

Texture component	Symbol
$\{001\}\langle 110\rangle$	
$\{114\}\langle 110\rangle$	
$\{112\}\langle 110\rangle$	
$\{111\}\langle 110\rangle$	
$\{111\}\langle 112\rangle$	

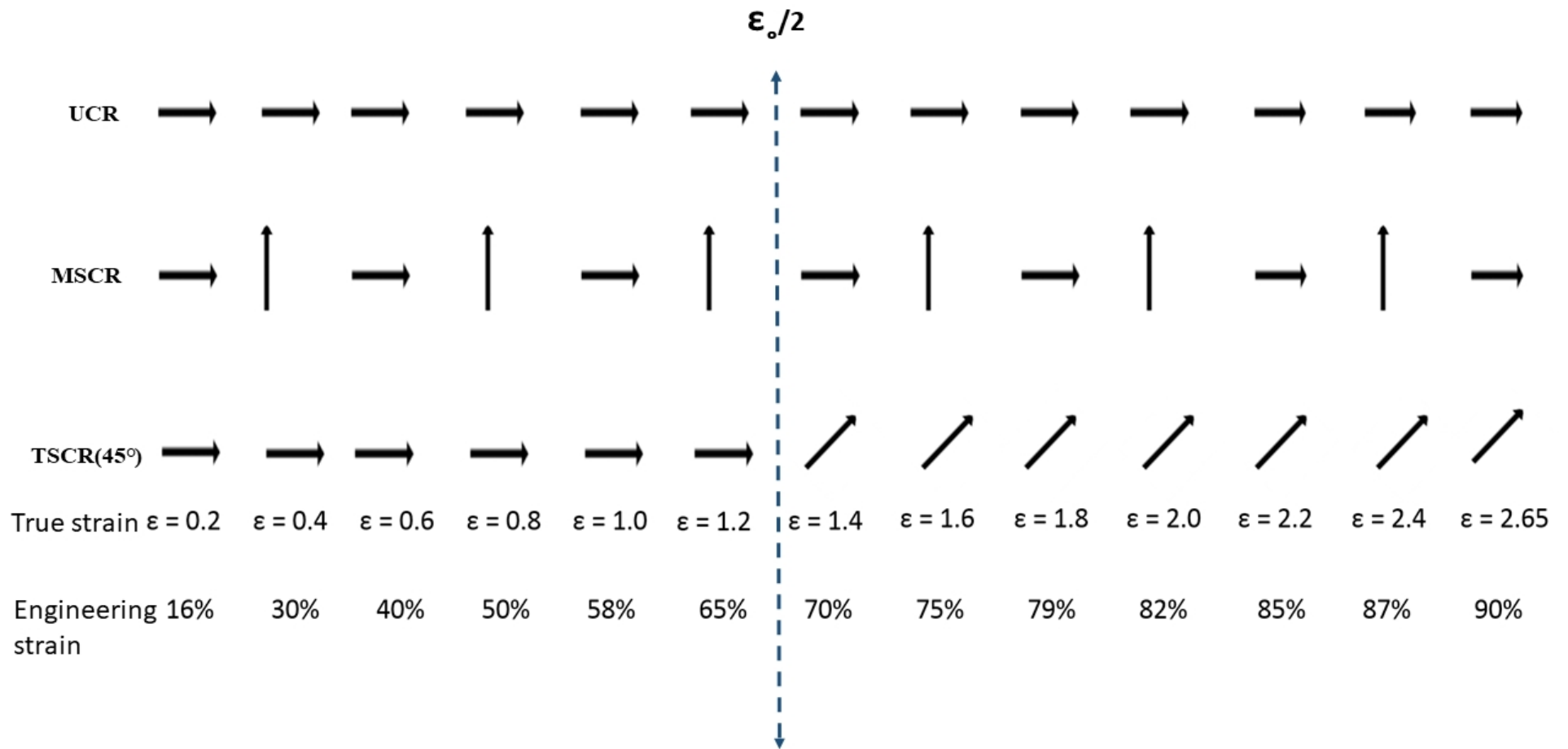


Fig.1: Schematic showing (a) UCR, (b) MSCR and (c) TSCR(45°) processing routes.

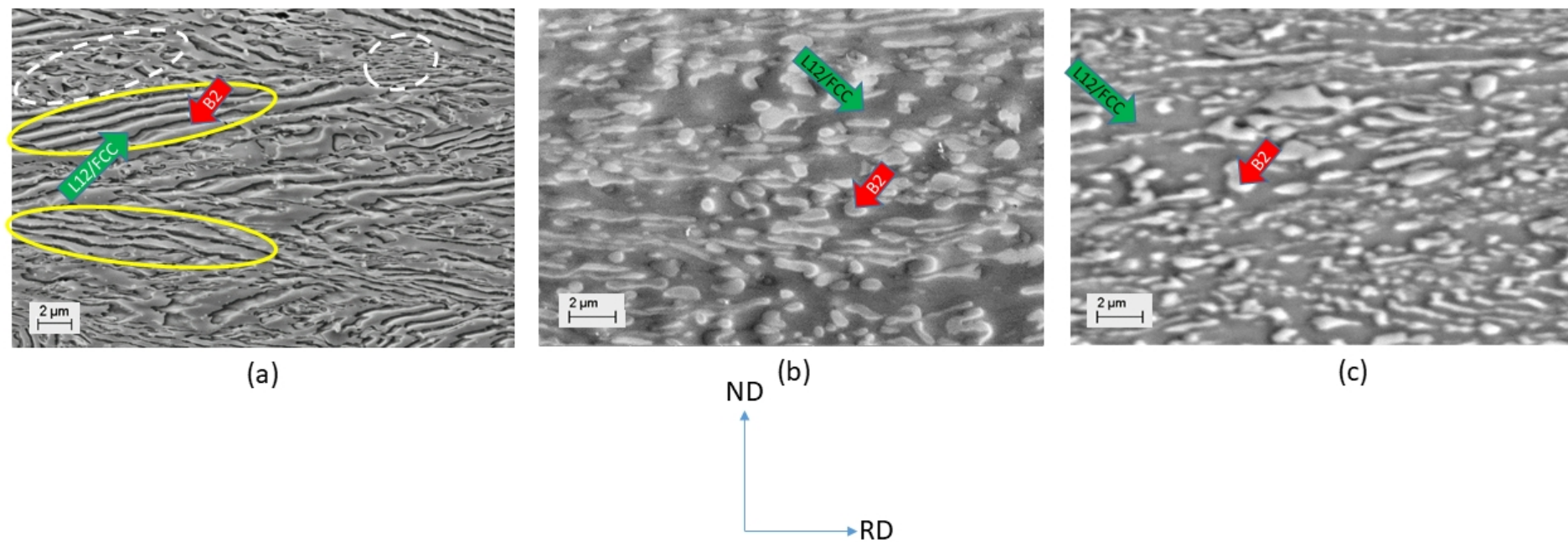


Fig.2: SEM micrographs of 90% cryo-rolled EHEA processed by (a) UCR, (b) MSCR and (c) TSCR(45°) processing routes.

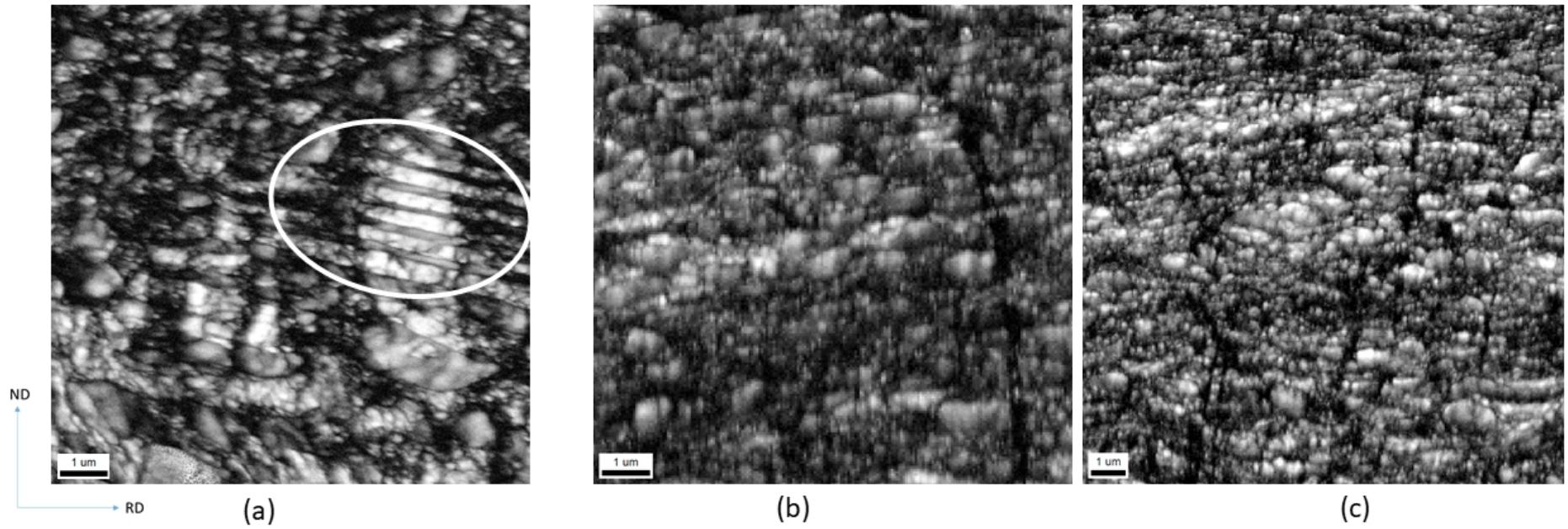


Fig.3: EBSD IQ maps of 90% cryo-rolled EHEA processed by (a) UCR, (b) MSCR and (c) TSCR(45°) processing routes.

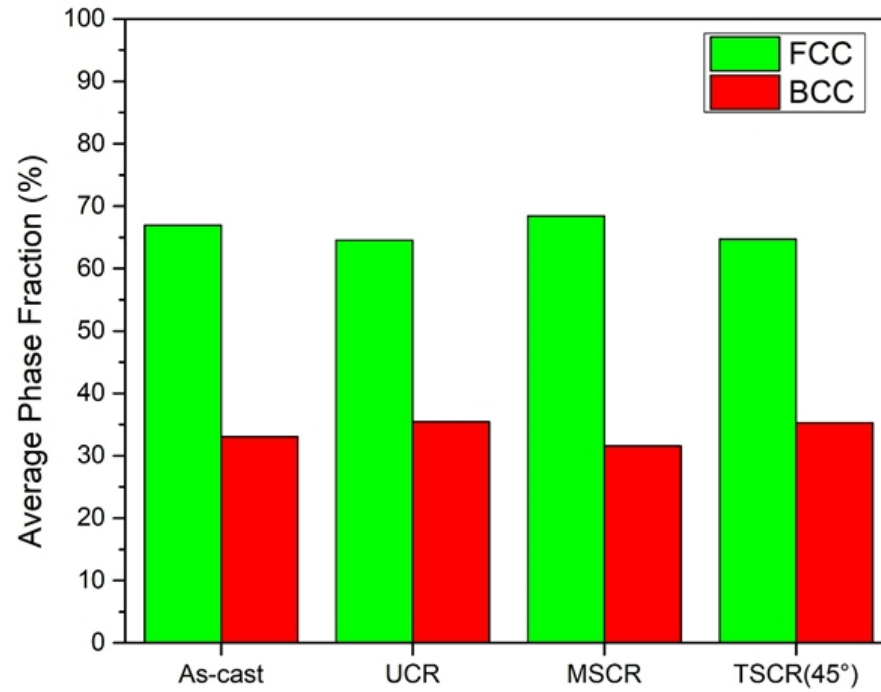


Fig.4: Phase fractions in as-cast and 90% cryo-deformed EHEA processed by different rolling routes.

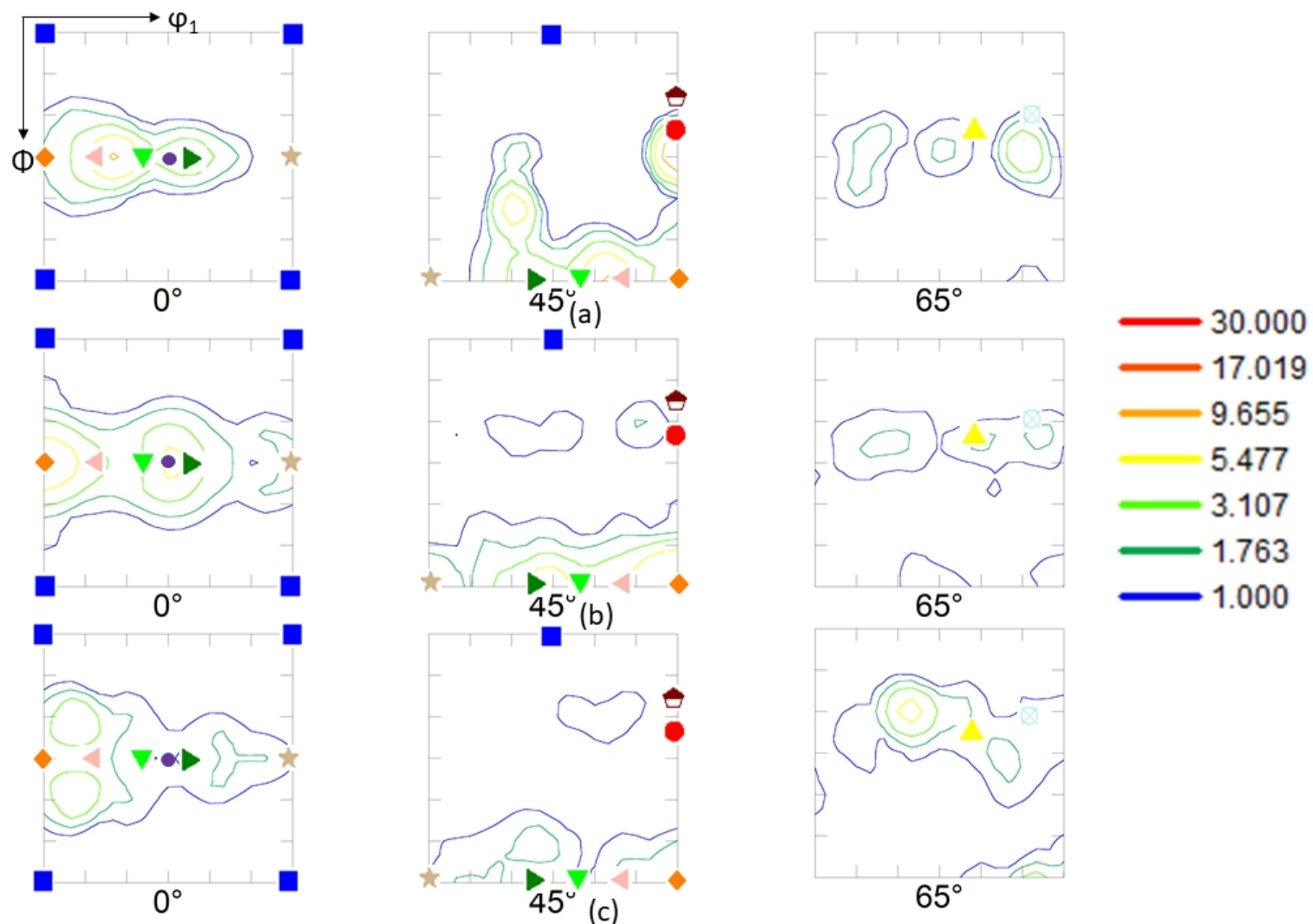


Fig.5: Relevant ODF sections of the L_{12}/FCC phase in 90% cryo-rolled EHEA processed by (a) UCR, (b) MSCR and (c) TSCR(45°) processing routes (for legends, refer to Table 1).

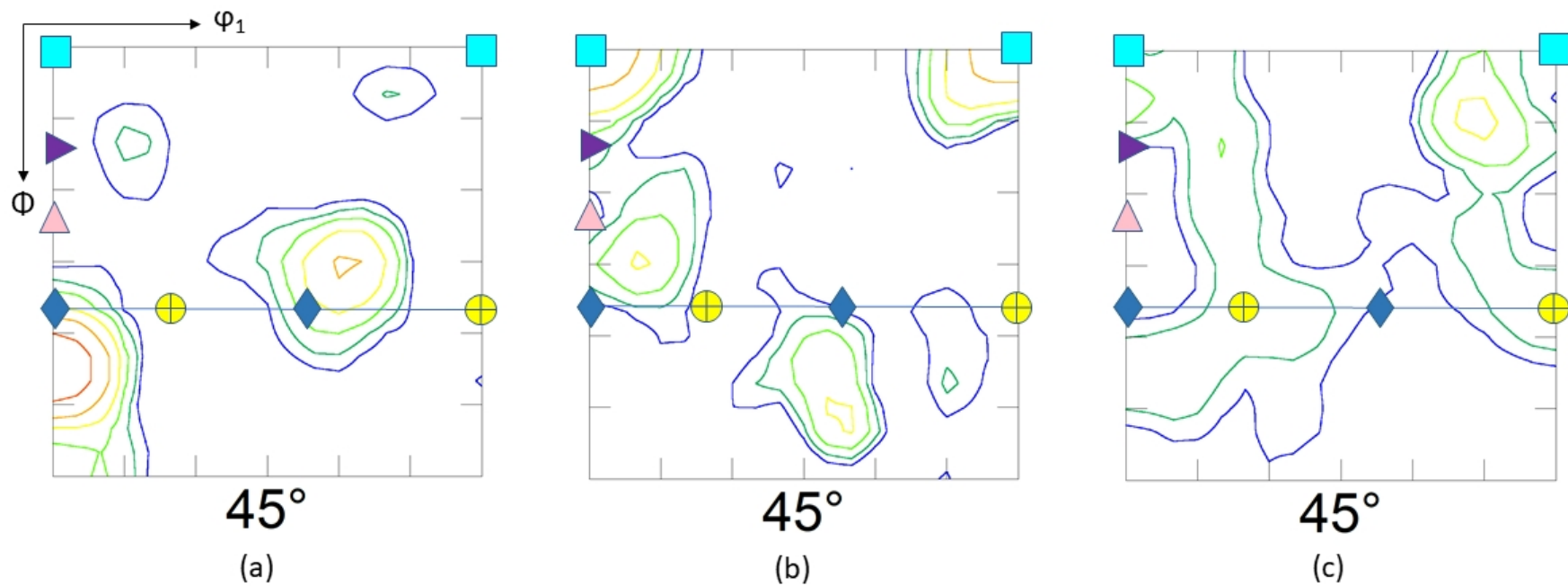


Fig.6: $\phi_2=45^\circ$ section ODFs of the B2 phase in 90% cryo-rolled EHEA processed by (a) UCR, (b) MSCR and (c) TSCR(45°) processing routes (for legends, refer to Table 2). The intensities of the contour lines are same as in Fig.5.

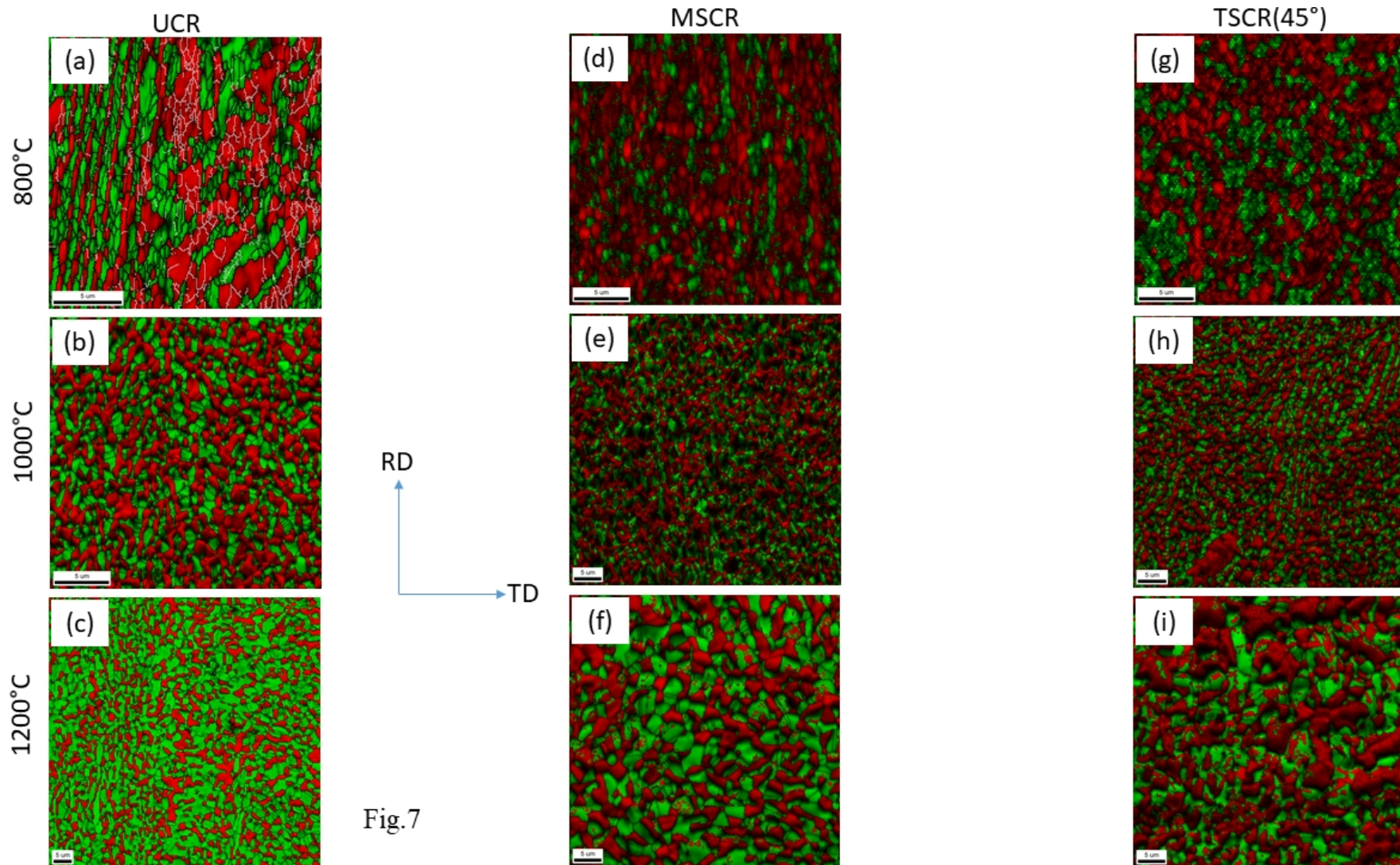
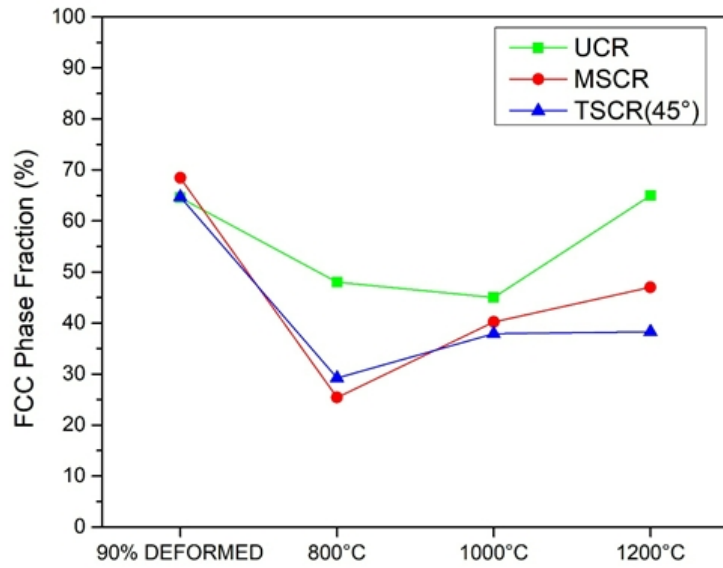
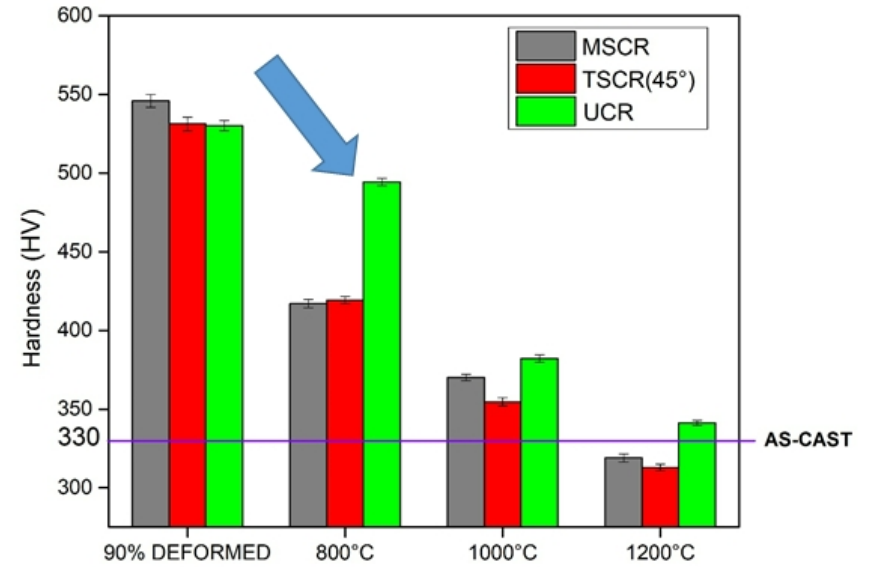


Fig.7



(a)



(b)

Fig.8: (a) Change in phase fraction and (b) hardness with annealing temperature in the EHEA processed by the three different routes.

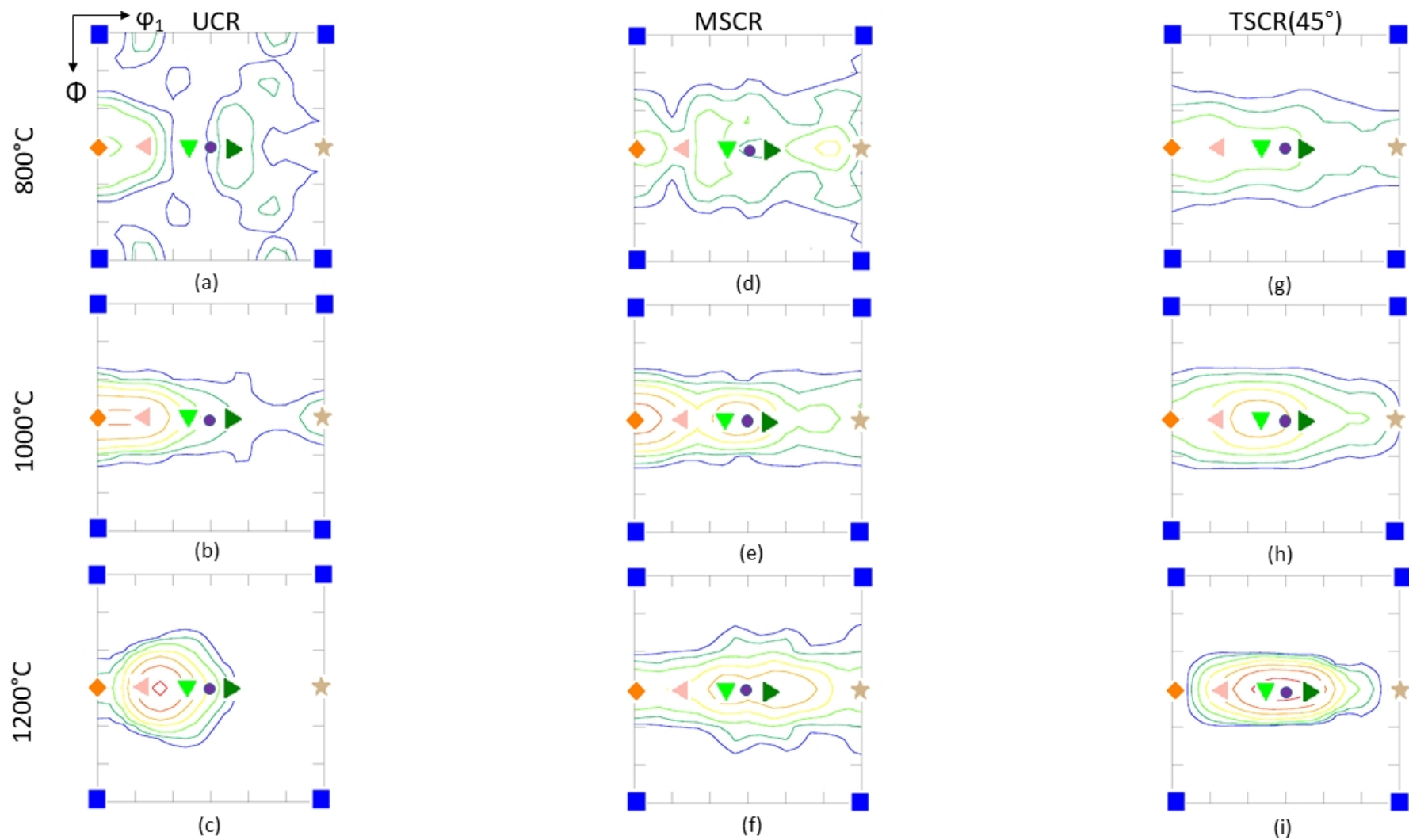


Fig.9: $\phi_2=0^\circ$ ODF sections of the L_{12}/FCC phase in annealed EHEA processed by different routes (for legends, refer to Table 1). The intensities of the contour lines are same as in Fig.5.

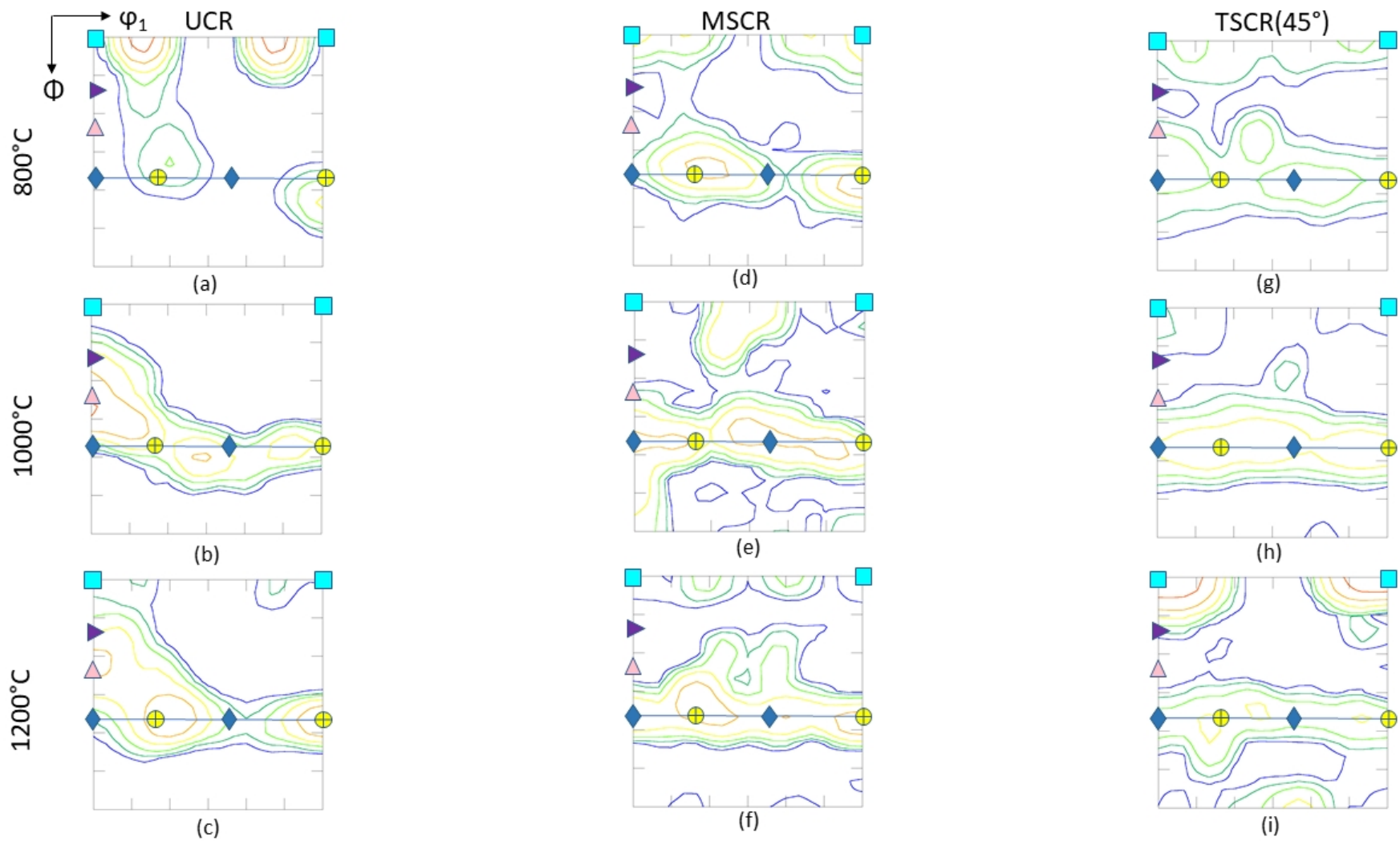


Fig.10: $\phi_2=45^\circ$ section of the ODFs of the B2 phase in annealed EHEA processed by different routes (for legends, refer to Table 2). The intensities of the contour lines are same as in Fig.5.